MIT Libraries | DSpace@MIT

MIT Open Access Articles

Quasielastic (e,e#p) reaction on [superscript]12C, [superscript 56]Fe, and [superscript 197]Au

Massachusetts Institute of Technology

Quasielastic $(e, e'p)$ reaction on ^{12}C, ^{56}Fe, and ^{197}Au

D. Dutta,[15,10,*] D. van Westrum,[4,†] D. Abbott,[22] A. Ahmidouch,[7] Ts. A. Amatuoni,[25] C. Armstrong,[24,‡] J. Arrington,[2,§]
K. A. Assamagan,[6,‖] K. Bailey,[1] O. K. Baker,[22,6] S. Barrow,[18] K. Beard,[6] D. Beatty,[18,‡] S. Beedoe,[14] E. Beise,[11] E. Belz,[4]
C. Bochna,[9] P. E. Bosted,[12] H. Breuer,[11] E. E. W. Bruins,[10] R. Carlini,[22] J. Cha,[6,¶] N. Chant,[11] C. Cothran,[23]
W. J. Cummings,[1] S. Danagoulian,[14] D. Day,[23] D. DeSchepper,[10] J.-E. Ducret,[21] F. Duncan,[11,**] J. Dunne,[22,¶] T. Eden,[6]
R. Ent,[22] H. T. Fortune,[18] V. Frolov,[19,††] D. F. Geesaman,[1] H. Gao,[9,10,*] R. Gilman,[22,20] P. Guèye,[6] J. O. Hansen,[1,‡]
W. Hinton,[6,‡] R. J. Holt,[9] C. Jackson,[14] H. E. Jackson,[1] C. Jones,[1] S. Kaufman,[1] J. J. Kelly,[11] C. Keppel,[22,6]
M. Khandaker,[13] W. Kim,[8] E. Kinney,[4] A. Klein,[17] D. Koltenuk,[18,‡‡] L. Kramer,[10,§§] W. Lorenzon,[18,‖‖] A. Lung,[2,‡]
K. McFarlane,[13,¶¶] D. J. Mack,[22] R. Madey,[6,7] P. Markowitz,[5] J. Martin,[10] A. Mateos,[10] D. Meekins,[22,‡] M. A. Miller,[9]
R. Milner,[10] J. Mitchell,[22] R. Mohring,[11] H. Mkrtchyan,[25] A. M. Nathan,[9] G. Niculescu,[6,a] I. Niculescu,[6,b]
T. G. O'Neill,[1] D. Potterveld,[1] J. W. Price,[19,c] J. Reinhold,[1,§§] C. Salgado,[13] J. P. Schiffer,[1] R. E. Segel,[15] P. Stoler,[19]
R. Suleiman,[7,d] V. Tadevosyan,[25] L. Tang,[22,6] B. Terburg,[9,e] T. P. Welch,[16] C. Williamson,[10] S. Wood,[22] C. Yan,[22] J.-C. Yang,[22]
J. Yu,[18] B. Zeidman,[1] W. Zhao,[10] and B. Zihlmann[23]

[1]*Argonne National Laboratory, Argonne, Illinois 60439, USA*
[2]*California Institute of Technology, Pasadena, California 91125, USA*
[3]*Chungnam National University, Taejon 305-764, Korea*
[4]*University of Colorado, Boulder, Colorado 80309, USA*
[5]*Florida International University, University Park, Florida 33199, USA*
[6]*Hampton University, Hampton, Virginia 23668, USA*
[7]*Kent State University, Kent, Ohio 44242, USA*
[8]*Kyungpook National University, Taegu, South Korea*
[9]*University of Illinois, Champaign-Urbana, Illinois 61801, USA*
[10]*Massachusetts Institute of Technology, Cambridge, Massachusetts 02139, USA*
[11]*University of Maryland, College Park, Maryland 20742, USA*
[12]*University of Massachusetts, Amherst, Massachusetts 01003, USA*
[13]*Norfolk State University, Norfolk, Virginia 23504, USA*
[14]*North Carolina A & T, Greensboro, North Carolina 27411, USA*
[15]*Northwestern University, Evanston, Illinois 60201, USA*
[16]*Oregon State University, Corvallis, Oregon 97331, USA*
[17]*Old Dominion University, Norfolk, Virginia 23529, USA*
[18]*University of Pennsylvania, Philadelphia, Pennsylvania 19104, USA*
[19]*Rensselaer Polytechnic Institute, Troy, New York 12180, USA*
[20]*Rutgers University, New Brunswick, New Jersey 08903, USA*
[21]*CE Saclay, Gif-sur-Yvette, France*
[22]*Thomas Jefferson National Accelerator Facility, Newport News, Virginia 23606, USA*
[23]*University of Virginia, Charlottesville, Virginia 22901, USA*
[24]*William and Mary, Williamsburg, Virginia 23187, USA*
[25]*Yerevan Physics Institute, Yerevan, Armenia*

We report the results from a systematic study of the quasielastic $(e, e'p)$ reaction on ^{12}C, ^{56}Fe, and ^{197}Au performed at Jefferson Lab. We have measured nuclear transparency and extracted spectral functions (corrected for radiation) over a Q^2 range of 0.64–3.25 $(\text{GeV}/c)^2$ for all three nuclei. In addition, we have extracted separated longitudinal and transverse spectral functions at Q^2 of 0.64 and 1.8 $(\text{GeV}/c)^2$ for these three nuclei (except for ^{197}Au at the higher Q^2). The spectral functions are compared to a number of theoretical calculations. The measured spectral functions differ in detail but not in overall shape from most of the theoretical models. In all three targets the measured spectral functions show considerable excess transverse strength at $Q^2 = 0.64$ $(\text{GeV}/c)^2$, which is much reduced at 1.8 $(\text{GeV}/c)^2$.

---

*Present address: Duke University, Durham, NC 27708.
†Present address: Micro-g Solutions Inc., Erie, CO 80516.
‡Present address: TJNAF, Newport News, VA 23606.
§Present address: Argonne Nat'l Lab, Argonne, IL 60439.

INTRODUCTION

The value of studying electronuclear reactions has long been recognized. In such studies the entire nucleus is accessed via a well-understood interaction. A new avenue of investigations has been opened up with the completion of the continuous beam, multi-GeV electron accelerator at the Thomas Jefferson National Accelerator Facility, also known as Jefferson Lab (JLab). The present paper reports results from the first experiment done at this facility, which is a study of $(e,e'p)$ reactions in the quasielastic region. This experiment utilized one of the advantages of electron scattering, namely, that the transferred energy and momentum can be varied separately, and one of the main features of JLab, namely, the high-intensity continuous electron beam of CEBAF which makes it possible to do coincidence measurements orders of magnitude more extensive than could be done previously.

The simplest model of a nucleus is one of independent nucleons populating the lowest available shell-model orbits. In a simple picture of e-p scattering within a nucleus, the electron scatters from a single proton which is moving due to its Fermi momentum. The struck proton may then interact with the residual A-1 nucleons before leaving the nucleus. Of course, neither the nucleus nor the scattering process are this simple and the deviations from these simple pictures reveal much about nuclei and their constituents, both real and virtual. The present experiment consisted of measuring proton spectra in coincidence with inelastically scattered electrons with the energy of the electrons chosen such as to be in the "quasielastic" region, i.e., at energies corresponding to scattering from single off-mass-shell nucleons. The spectra were taken in an angular region about the "conjugate" angle, i.e., the angle for scattering from stationary nucleons, over an angular range sufficient to cover the smearing of the two-body kinematics caused by the Fermi momentum of the confined protons. Data were taken over the range $0.64 < Q^2 < 3.25$ (GeV/c)^2 where Q^2 is the square of the four-momentum transferred to the struck proton.

‖Present address: Brookhaven Nat'l Lab, Upton, NY 11973.

¶Present address: Mississippi State University, Mississippi State, MS 39762.

**Present address: Queens University, Kingston, Ontario, Canada.

††Present address: University of Minnesota, Minneapolis, MN 55439.

‡‡Present address: Lincoln Labs, MIT, Lexington, MA 02420.

§§Present address: Florida International University, Miami, FL 33199.

‖‖Present address: University of Michigan, Ann Arbor, MI 48109.

¶¶Present address: Hampton University, Hampton, VA 23668.

aPresent address: University of Virginia, Charlottesville, VA 22901.

bPresent address: James Madison University, Harrisonburg, VA 22807.

cPresent address: University of California, Los Angeles, CA 90095.

dPresent address: MIT, Cambridge, MA 02139.

ePresent address: General Electric Corp., Cleveland, OH 44114.

For an electron knocking a proton p out of a nucleus A with energy transfer ω and (three) momentum transfer $\vec{q}$ leaving a scattered proton p' and a residual nucleus $A-1$, two important kinematic quantities are the missing energy

$$E_m = \omega - T_{p'} - T_{A-1} \tag{1}$$

and missing momentum

$$\vec{p}_m = \vec{p}_{p'} - \vec{q}, \tag{2}$$

where $T_{p'}$ and T_{A-1} are the kinetic energies of the knocked-out proton and recoiling nucleus, respectively. The spectral functions were extracted from the E_m and $\vec{p}_m$ spectra and compared to a variety of theoretical calculations. The total $(e,e'p)$ yields are obtained by integrating over the spectral functions and the transparencies then determined by comparing these yields with those predicted by plane wave impulse approximation (PWIA) calculations. Because the PWIA does not allow for final-state interactions the ratio of measured to calculated yield should just be the fraction of outgoing protons which do not suffer a final-state interaction and this is what is defined to be the transparency. Determinations of nuclear transparencies using the $(e,e'p)$ reaction have been reported for a range of targets covering the periodic table, at Bates for $Q^2 = 0.34$ (GeV/c)^2 [1], at SLAC for Q^2 between 1 and 7 (GeV/c)^2 [2,3], and more recently at JLab between 3 and 8.1 (GeV/c)^2 [4]. The present work maps out regions not previously covered and is of greater statistical accuracy. Longitudinal-transverse (L-T) separations were performed at two values of Q^2 from which the first reported extensive separated spectral functions are obtained. Some transparency results from the present experiment have been previously published [5], as have the separated spectral functions for carbon [6].

The differential cross section for elastic electron-proton scattering is given by the well-known Rosenbluth formula:

$$\frac{d\sigma}{d\Omega} = \left(\frac{d\sigma}{d\Omega}\right)_{\text{Mott}} \frac{Q^2}{|\vec{q}|^2}[G_E^2(Q^2) + \tau\epsilon^{-1}G_M^2(Q^2)], \tag{3}$$

where $(d\sigma/d\Omega)_{\text{Mott}}$ is the differential cross section for the scattering of an electron off a unit point charge, $\epsilon = 1/[1 + 2(1+\tau)\tan^2(\theta/2)]$ is the virtual polarization parameter, $\tau = |\vec{q}|^2/Q^2 - 1$, G_E is the proton electric form factor, and G_M is the proton magnetic form factor in units of the nuclear magneton $e\hbar/2M_p$ where M_p is the proton mass.

The L-T separation is performed by measuring the cross section at different values of ϵ while keeping Q^2 constant, thus permitting the extraction of G_E and G_M.

In scattering from a nucleus the cross section is expressed in terms of four response functions and in the PWIA the coincidence $(e,e'p)$ cross sections can be written as

$$\frac{d^6\sigma}{dE_{e'}d\Omega_{e'}dE_{p'}d\Omega_{p'}}$$

$$= p' E_{p'} \sigma_{\text{Mott}} \left\{ \lambda^2 W_L(q, \omega) + \left[\frac{\lambda}{2} + \tan^2\left(\frac{\theta}{2}\right) \right] W_T(q, \omega) \right.$$

$$+ \lambda \left[\lambda + \tan^2\left(\frac{\theta}{2}\right) \right]^{1/2} W_{LT}(q, \omega)\cos(\phi)$$

$$\left. + \frac{\lambda}{2} W_{TT}(q, \omega)\cos(2\phi) \right\}, \tag{4}$$

where $\lambda = Q^2/|\vec{q}|^2$, θ is the scattering angle, and ϕ is the azimuthal angle between the scattering plane and the plane containing $\vec{q}$ and $\vec{p}'$.

The physics of interest is contained in the four response functions W_L, W_T, W_{LT}, and W_{TT}. Both of the interference terms, W_{LT} and W_{TT}, are proportional to $\sin\gamma$, where γ is the angle between the scattered proton and the transferred momentum $\vec{q}$. Therefore, when measurements are made along $\vec{q}$, i.e., in "parallel kinematics," the interference terms are absent. Varying the incident energy makes it possible to vary θ at constant q and ω and thus disentangle W_L and W_T, that is, perform an *L-T* separation. Although, the position of the spectrometers allowed measurements only in the scattering plane, the interference term W_{LT} could be investigated by varying the proton angle about the direction of $\vec{q}$. Measurements were taken by varying both θ and γ. This is the first *L-T* separation measured for quasielastic $(e, e'p)$ scattering that covers a large range in both A and Q^2.

The free electron-proton elastic cross sections play a central role in interpreting much of the data in the present work. They are used in the determination of nuclear transparency, in the extraction of the separated spectral functions, as well as in the determination of the spectrometers' acceptances. Unless otherwise noted, the proton electric form factor G_E is taken to have the dipole form,

$$G_E = \left(1 + \frac{Q^2}{0.71} \right)^{-2}, \tag{5}$$

and the magnetic form factor G_M is taken from the Gari-Krümpelmann [7] parametrization, which, to a good approximation [better than 4% for $Q^2 < 2.0$ (GeV/$c)^2$] [8], yields $G_M = \mu_p G_E$. Rosenbluth separation measurements of *e-p* scattering [9,10] support the validity of this relationship.

In recent years a series of experiments have been performed [11,12] in which the ratio $\mu_p G_E/G_M$ is determined by measuring the direction of the polarization vector of the protons scattered by a longitudinally polarized electron beam. In contrast to the Rosenbluth separation results, these experiments find G_E/G_M decreasing approximately linearly with Q^2 out to at least $Q^2 = 5.6$ (GeV/$c)^2$. The ratio $\mu_p G_E/G_M$ was found to be approximately 0.79 at 1.8 (GeV/$c)^2$, where one of the present *L-T* separations was performed. At the other momentum transfer where an *L-T* separation was performed, 0.64 (GeV/$c)^2$, this ratio was found to be about 5% less than

the $Q^2 = 0$ value of unity. The implications of the polarization transfer results for the present work are discussed in the section on *L-T* separations.

EXPERIMENT

Electron beam

The experiment was performed in 1995-1996 in Hall C at JLab and was the first experiment performed at the Laboratory. Data were taken at (nominal) electron energies $E_e = (0.8N + 0.045)$ GeV with $N = 1-4$ representing the number of "passes" the electrons made around the accelerating track. The absolute beam energy was determined at one-pass by two independent methods. One method (described in detail in Ref. [13]) is to use the inelastic scattering to an excited state whose energy is accurately known to calibrate the dispersion of a spectrometer and then use the calibrated spectrometer to measure the energy of the scattered electron as a function of nuclear target mass. For these measurements a carbon target was used and the dispersion determined by measuring the difference in position of the electrons scattered to the ground and the $4.438\,91 \pm 0.000\,31$ MeV [14] first excited state. A BeO target was then substituted and the energy of the beam, E, determined using the formula

$$\Delta E_{\text{recoil}} = 2E^2 \sin^2\frac{\theta}{2}\left(\frac{1}{M_1} - \frac{1}{M_2} \right). \tag{6}$$

One can accurately determine ΔE_{recoil} because once the dispersion has been accurately measured the only unknown in Eq. (6) is the beam energy E. This procedure was repeated for several values of the spectrometer magnetic field. With both targets a small correction was made for the energy loss of the electrons in the target.

The other method is to determine the angle of the diffraction minimum for scattering to a state where the position can be accurately calculated. The minimum for scattering to the ^{12}C ground state is known to be at $Q^2 = 0.129$ (GeV/$c)^2$ [15]. The (four) momentum transfer can be written as

$$Q^2 = 4EE'\sin^2\frac{\theta}{2}, \quad E' = \frac{E}{1 + \dfrac{2E\sin^2\dfrac{\theta}{2}}{M}}, \tag{7}$$

where M is the mass of the scattering nucleus and θ is the electron scattering angle. An improvement in accuracy in the measurement of Q is obtained by using the ratio of elastic scattering to inelastic scattering. Again, then, the only unknown is the incident electron energy E. The two methods agreed to 1 part in 2000 and the absolute energy determination using these methods is believed to be accurate to 10^{-3}. These methods become less feasible as the energy is increased. The beam energy can also be determined by measuring the energy and angle of the scattered particles in electron-proton elastic scattering. Because of the uncertainties in the angle and momentum measurements this method is less accurate than the other two but has the advantage that it can be used over the entire range

of incident electron energies. Elastic *e-p* scattering was used to measure the energy of the three-pass beam with an uncertainty of 1 part in 500. Beam energy was also determined by measuring the magnetic field needed to bend the beam around the Hall C arc. The energy calibration as well as other aspects of the experiment are discussed more completely elsewhere [16].

Beam currents of 10 to 60 μA were used. The currents were monitored by three microwave cavities that were installed for this purpose in the Hall C beam line [17]. The absolute calibration was performed by comparison with an Unser cavity, which is a parametric dc current transformer with very stable gain but a drifting offset which was determined as part of our daily calibration procedure. The overall accuracy in the beam current measurement was ±1%.

Targets

Data were taken with ≈200 mg/cm^2 C, Fe, and Au targets mounted on a steel ladder in an aluminum scattering chamber. The target thicknesses were determined to about 0.1%. The *e-p* elastic scattering data used for calibration were taken using the 4.0 cm cell of the Hall C cryogenic target [18]. During the early part of the experiment, before the cryogenic target was available, some data were taken with a solid CH$_2$ target but these data were only used to check some kinematic offsets. The compositions of hydrocarbon targets are subject to change under beam irradiation and therefore all the calibration data were taken with the liquid hydrogen target. The cryogenic targets are also mounted on a ladder with both ladders contained in the aluminum scattering chamber. The 123.0 cm diameter scattering chamber has entrance and exit snouts for the beam and several pumping and viewing ports. The particles that went to the high-momentum spectrometer (HMS) exited through a 0.4 mm aluminum window and those to the short orbit spectrometer (SOS) through a 0.2 mm aluminum window. For both spectrometers the particles had to pass through about 15 cm of air before entering the spectrometer.

Spectrometers

Data were taken with the HMS and the SOS in coincidence. This experiment served as the commissioning experiment for these spectrometers. The HMS detected the electrons and the SOS the protons, except at the highest Q^2 where the roles of the spectrometers were reversed.

High-momentum spectrometer

The HMS is a 25° vertical bend spectrometer made up of superconducting magnets in a *QQQD* configuration. The dipole field is monitored and regulated with an NMR probe and kept constant at the 10^{-4} level. The spectrometer rotates on a pair of rails between 12.5° and 90° with respect to the beam line. The HMS maximum central momentum is 7.3 GeV/*c* and in preparing for the present experiment the spectrometer was tested up to 4.4 GeV/*c*, although the highest setting at which data were taken was 2.6 GeV/*c*. The usable momentum bite of the spectrometer is ≈20%. A mo-

mentum resolution (σ) of $<1.4\times10^{-3}$, and an in-plane (out-of-plane) angular resolution of 0.8 (1.0) mrad was achieved for the HMS. With no collimator in place the solid angle subtended for a point target is 8.1 msr. A 6.35 cm thick HEAVYMET (machinable Tungsten alloy, 10% Cu and Ni; density=17 g/cm^3) collimator with a flared octagonal aperture limited the solid angle to 6.8 msr. The higher momentum particles were usually detected in the HMS and except at the backward (electron) angles these were the electrons. Detailed information about the HMS can be found in Ref. [19].

Short orbit spectrometer

The SOS consists of three (normal conducting) magnets in a $Q\overline{DD}$ configuration. The deflection is vertical with the net bend of 18° at the central momentum. The magnetic fields are monitored with Hall probes. With its short path length of 11 m this spectrometer is particularly well suited for detecting short-lived particles, though obviously this attribute was not used in the present experiment. The spectrometer can be moved between 13.1° and 168.4° with respect to the beam line (in this experiment the minimum angle was 14.5°) and can be moved up to 20° out of the horizontal plane, though this was not done in this experiment. The spectrometer maximum central momentum is 1.8 GeV/*c* with a nominal momentum bite of 40%. A momentum resolution (σ) of $<1.0\times10^{-3}$, an in-plane (out-of-plane) angular resolution of 4.5 (0.5) mrad was achieved for the SOS. The solid angle subtended is ≈9 msr for a point target, although a collimator similar to that used with the HMS limited the solid angle to 7.5 msr. As with the HMS, further details about the SOS can be found in the spectrometer documentation [19,20].

Detector stacks

The detector stacks in the two spectrometers are virtually identical. The particles pass through, in order, a set of drift chambers, a pair of hodoscopes, a gas Čerenkov detector, another pair of hodoscopes, and then a lead-glass calorimeter. The particle velocity is inferred from the time of flight between the two pairs of hodoscopes, though the spectra proved to be so clean that it was not necessary to use time of flight for particle identification. Signals from the hodoscope planes provide the trigger and in the electron arm particle identification can be incorporated into the trigger by requiring a signal from the Čerenkov counter and/or a sufficiently large pulse from the calorimeter. Coincidences between the triggers selected out the $(e,e'p)$ events that make up the physics data.

The drift chambers serve to determine the particles' position, $x(y)$, and direction, $x'(y')$, in the bend (nonbend) plane of the spectrometer and it is these quantities that are used to reconstruct the events. Each spectrometer has two chambers and each chamber contains six planes of wires. In each HMS chamber one pair measures x, one pair measures y, and the remaining two planes are rotated ±15° with respect to the x plane. The purpose of the third pair of planes is to correlate the xy information when more than one particle traverses a chamber during the readout interval. In the SOS chambers

one pair is in the x plane and the other two pairs of planes are at $\pm 60°$ with respect to the x plane. Position resolution per plane is <250 μm in the HMS chambers and <200 μm in the SOS. The wire chamber data were used to reconstruct the trajectory of the particles and determine the particles momentum fraction relative to the central momentum, $\delta p/p$.

Wire chamber tracking efficiency is an important element in the overall system efficiency and, as such, must be accurately measured. This was done by using the position information in the hodoscopes to tag particles passing through a small central region of the chambers and then see what fraction of such events was reconstructed from the wire chamber signals. In both spectrometers typical tracking efficiency was greater than 97%, which was determined to better than 1%. The main sources of wire chamber tracking inefficiency are inefficiencies in the chambers themselves (we require that five of the six planes have good hits) and inefficiency in the reconstruction algorithm. The measured inefficiency was the sum of these inefficiencies and no attempt was made to disentangle the two.

Calibrations

Spectrometer optimizations

Because this was the first experiment performed in Hall C, considerable effort went into first optimizing the performance of the spectrometers and then optimizing the data analysis so as to achieve the highest possible accuracy. The magnetic field of the HMS quadrupoles was mapped to determine its optical axis and its effective field length versus current, with effective field length defined as the line integral of the field divided by the average field. However, the HMS dipole was not mapped but, rather, its magnetic field to current (B-to-I) relation was calculated using the TOSCA program [21]. The measured field map of the quadrupole and the TOSCA generated map of the dipole were used to build an optics model of the spectrometer with the COSY program [22]. For a desired magnetic field of the dipole (i.e., a desired central momentum) the dipole current was set according to the B-to-I relation predicted by the TOSCA program, while the COSY model was used to get the starting value of the quadrupole to dipole ratio (Q/D). The Q/D ratio was then varied to get the best focus in the spectrometer and these optimized ratios were used to determine the current settings of the quadrupole for a desired central momentum of the spectrometer. From elastic e-p scattering data it was later determined that the B-to-I relation of the dipole predicted by TOSCA was low by about 0.9%. The dipole currents were adjusted accordingly to correct for this difference. A similar procedure was followed for the SOS except that the quadrupole was not mapped and the optics model was formulated using the COSY program assuming the field of the quadrupole magnet to be an ideal quadrupole. The SOS dipole B-to-I relation was also found to be slightly low (0.55%) and suitable corrections were made to the setting procedure.

The basic strategy in determining the momentum and direction of the scattered particles is to use the wire chamber data to determine the position (x, y) and the angles (x', y') of the particles at the focal plane which, in turn, specifies the trajectory of the particle through the spectrometer. This, of course, requires knowing the fields of the spectrometer, which are represented by a set of matrix elements that relate the position and direction of the particles as they cross the focal plane, to the particle's momentum, angles of emission, and starting position along the beam direction. The accuracy of the final results then depends on how well the matrix elements simulate the spectrometers and hence a great deal of effort went into optimizing these matrix elements.

The COSY program was used to calculate an initial set of reconstruction matrix elements using the mapped fields for the HMS magnets and the SOS dipoles and an assumed pure quadrupole field for the SOS quadrupole. The Hall C matrix element optimization package CMOP [23] was used to optimize the reconstruction matrix elements. In this package the dispersion matrix elements are optimized using momentum scans, i.e., varying the central momentum by varying the magnetic fields. For each spectrometer these momentum scans were performed for both elastic $p(e, e')$ and elastic ^{12}C(e, e') scattering. In order to obtain the angular matrix elements sieve slits, which are collimators containing accurately positioned holes, were placed in front of each of the spectrometers so that rays of known initial position and direction could be traced. The angular matrix elements were then fit by the CMOP package (using singular value decomposition method) to accurately reproduce the known positions of the sieve slit holes. Similarly the target y position (projection of the target length along the beam) reconstruction was optimized by utilizing the CMOP package with data from scans along the beam direction. These scans were performed by raising and lowering a slanted carbon target and the continuum portion of the carbon spectrum was used. Most of these calibration data were taken at one-pass, 845 MeV, with a check for reproducibility made with two-pass, 1645 MeV, electrons.

Acceptances

The spectrometer's acceptances were studied with the aid of the simulation code SIMC, which is an adoption to the JLab Hall C spectrometers of the $(e, e'p)$ simulation code written for SLAC experiment NE18 [24]. This simulation package employs models for each of the spectrometers (HMS and SOS). The same models were also used to study the optical properties of the spectrometers. These models use COSY generated sets of matrices to simulate the transport of charged particles through the magnetic field of the spectrometer to each major aperture of the spectrometer. Energy loss and multiple scattering in the intervening material were also included. The events that passed through all apertures were then reconstructed back to the target using another set of matrices generated by COSY. Surviving events were assigned a weight based on the PWIA cross section, radiative corrections, and Coulomb corrections. The PWIA cross section was calculated using the deForest [25] prescription σ_{cc1} for the off-shell e-p cross section and an independent particle shell model (IPSM) spectral function for the target nucleus involved. The PWIA calculations and the IPSM spectral functions are elaborated in the following two sections. The radiative corrections in SIMC were performed according to
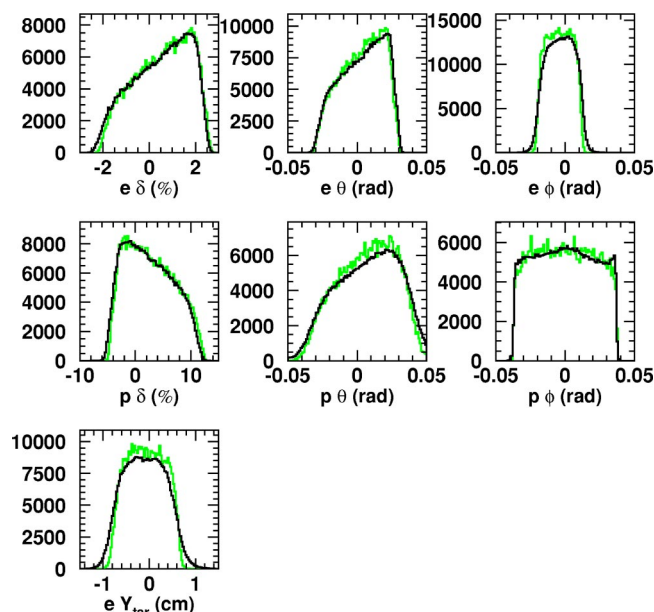
FIG. 1. (Color online) Comparison of calculated (dark line) and measured (light line) distributions. Top row depicts momentum, angle, and out-of-plane angle for electrons and the middle row the same for protons. Last picture depicts the projection of the distribution along the target for electrons.

the Mo and Tsai [26] formulation adapted for the coincidence $(e, e'p)$ reaction as described in Ref. [27]. Further, a normalization factor was calculated from the experimental luminosity, phase space volume, and the total number of events generated, so that the simulation provided a prediction of the absolute yield.

The reconstructed momentum, scattering angle, out-of-plane angle, and target length distributions generated by the model were compared with the distributions obtained from the e-p elastic scattering data as shown in Fig. 1. These results are an indicator of how well the model acceptance simulated the true acceptance of the spectrometer.

Corrections

Radiative corrections

A major issue in electron scattering experiments is radiative corrections. The incoming and outgoing electrons can interact with the Coulomb field of the nucleus involved in the scattering which results in the emission and absorption of virtual photons and emission of real, primarily soft, photons. Formulas for correcting for these radiative losses have been worked out by Mo and Tsai [26]. Correcting spectral functions deduced from $(e, e'p)$ coincidence spectra is considerably more complicated because in this case the radiated momentum as well as the lost energy must be allowed for. Although these are real physical processes, they are experiment specific and so most theoretical calculations do not take them into account. The prescription for doing this for coincidence $(e, e'p)$ reactions developed by Ent *et al.* [27] was used in the present work. Using this prescription, radiated spectra are generated which can be directly compared with

the experimentally measured spectra. This point is discussed further in the section on spectral functions.

Nuclear reactions

Protons, being hadrons, will undergo strong interactions in traversing the detector stack and valid coincidences will be lost. This loss was measured directly using e-p elastic scattering. Each scattered electron must have an accompanying proton and electrons were selected from a small region at the center of the acceptance, thus ensuring that protons could only be lost through nuclear interactions and other spectrometer inefficiencies. Transmissions of close to 95% were measured for both spectrometers, consistent with calculations of absorbtion of protons in the traversed material, and believed to be known to 1%. The absorption is virtually constant over the range of proton energies encountered in this experiment and therefore the small uncertainty in the absorption has little effect on any of the results.

Deadtimes

There were two data acquisition deadtimes of possible concern: electronic deadtime and computer deadtime. Electronic deadtime occurs when triggers are not counted because the electronics hardware is busy processing previous triggers. Electronic deadtime is dependent on the width of the logic signals, which for nearly all of the gates was 30 ns. This deadtime was measured by recording the rates of multiple copies of the trigger with varying widths and then extrapolating to the rate at zero width. For both spectrometers the electronic deadtime was found to be <0.1%. Computer deadtime is a more serious matter. Most of the earlier data were taken in nonbuffered mode where the processing time was about 400 μs. Later data were taken in the buffered mode with processing times of about 75 μs. Over 80% of the data were taken with deadtimes of <10% but there were a few runs where deadtimes were as great as 60%. Even in these extreme cases the loss of event is known to better than 0.5% from the ratio of the number of triggers generated to the number of triggers recorded by the data acquisition. This method was checked by measuring a large rate run and then varying the fraction of triggers recorded by the data acquisition.

RESULTS

Kinematics

Table I shows the kinematics settings where data were taken. The protons in the nucleus have finite momentum and therefore the struck protons from quasielastic scattering will emerge in a cone about the three-momentum transfer $\vec{q}$ and measurements must be taken across this cone. The lower the magnitude of $\vec{q}$, the broader the cone but, fortunately, the cross section increases with decreasing Q^2. While it is desirable to take data over as large a range of Q^2 as possible the cross section falls off so rapidly with increasing Q^2 that at the highest Q^2 point, 3.25 (GeV/c)^2, the cross section is so small that data could only be taken on one side of the conjugate angle. *L-T* separations were performed at Q^2 of

TABLE I. Table of kinematics for experiment E91-013. The central proton angles in bold represent the conjugate angle.

Beam energy (GeV)	Central electron energy (GeV)	Central electron angle (deg)	Central proton energy (MeV)	Central proton angle (deg)	Q^2 (GeV²/c^2)	ϵ
2.445	2.075	20.5	350	36.4,39.4 43.4,47.4 51.4,**55.4** 59.4,63.4 67.4,71.4 75.4	0.64	0.93
0.845	0.475	78.5	350	27.8 **31.8** 35.8,39.8, 43.8,47.8	0.64	0.38
3.245	2.255	28.6	970	32.6,36.6, **40.6**, 44.6,48.6, 52.6	1.80	0.83
1.645	0.675	80.0	970	**22.8**, 26.8,30.8 34.8	1.83	0.31
2.445	1.725	32.0	700	31.5,35.5 39.5,**43.5** 47.5,51.4 55.4	1.28	0.81
3.245	1.40	50.0	1800	**25.5** 28.0,30.5	3.25	0.54

0.64 (GeV/c)^2 and 1.8 (GeV/c)^2. In order to get a good separation, data should be taken at as divergent values of ϵ [Eq. (1)] as possible, which translates into a large ϵ point at small (electron) angle and large incident energy and a low ϵ point at large angle and small energy (Table I). The cross section decreases rapidly with increasing angle and so it was only possible to cover one side of the proton cone at ϵ =0.31, Q^2=1.8 (GeV/c)^2 and even at Q^2=0.64 (GeV/c)^2 there was time for only one point on the low-angle side of the cone. Furthermore, no gold data were taken at the larger angle and higher Q^2 (1.8 (GeV/c)^2).

Spectral functions

In the plane wave impulse approximation the cross section can be factorized into a product of an elementary electron-proton cross section σ_{ep} and a nuclear spectral function $S(E_s,\vec{p}_m)$, i.e.,

$$\frac{d^6\sigma}{dE_{e'}d\Omega_{e'}d^3p'} = K\sigma_{ep}S(E_s,\vec{p}_m), \qquad (8)$$

where K is just a kinematic factor. The spectral function for protons in a nucleus $S(E_s,\vec{p}_m)$ is defined as the prob-
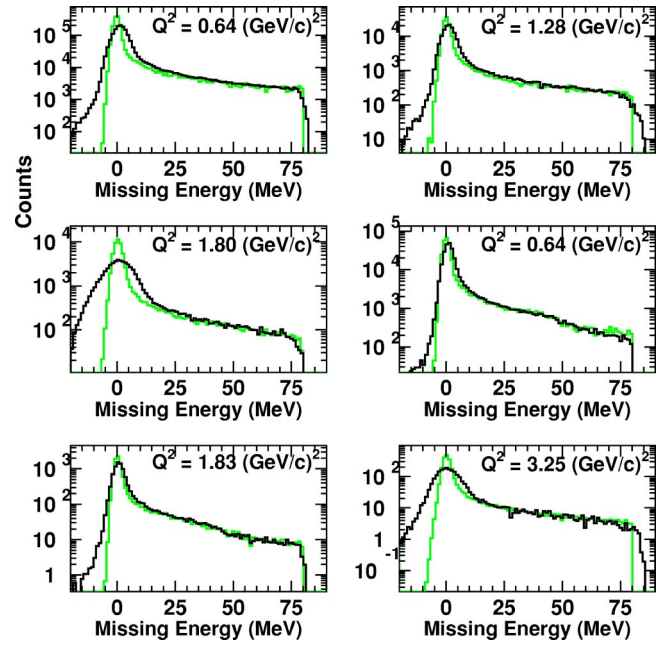

FIG. 2. (Color online) Measured missing energy spectra for hydrogen (dark line) compared to spectra calculated using the Monte Carlo code SIMC (light line). The top left and middle right panels refer to the forward and backward electron angle kinematics, respectively, at Q^2=0.64 (GeV/c)^2 and the middle left and bottom left panels refer to the forward and backward electron angle kinematics, respectively, at Q^2=1.80 (GeV/c)^2. These are the L-T separation kinematics.

ability of finding a proton with separation energy E_s and momentum $\vec{p}_m$ inside that nucleus. Obtaining spectral functions was a major objective of the present work and this section details how the spectral functions were deduced from the measured missing energy and missing momentum spectra.

Hydrogen data

A missing energy and a missing momentum spectrum were obtained at each data point. For the hydrogen target this served as a measure of the response of the system while for the other targets these are the spectra from which the spectral functions are determined. Hydrogen missing energy spectra along with the Monte Carlo calculated spectra at the various kinematics are shown in Fig. 2. The fact that the low-energy tail is well reproduced out to the highest missing energy accepted (80 MeV), shows that the radiative corrections are being handled correctly. Missing energy resolution, which is not of primary importance in the present work, is clearly not well incorporated into the code in that the calculated zero missing energy peak is always narrower than that observed. The peaks get broader with increasing energy of the scattered particle (see Table I), as could be expected, and this effect is not adequately accounted for. The effect is most dramatic at the two values of Q^2 where data were taken at two different electron angles, and the peak is much broader at the forward angle where the electron energy is higher, while the proton energy remains the same. The missing energy resolution

TABLE II. Ratio of observed to predicted yield for *e-p* elastic scattering. Uncertainties are statistical only, except for the $(e, e'p)$ point at 3.25 $(GeV/c)^2$ where there is an additional systematic uncertainty that is discussed in the text.

Q^2 $(GeV/c)^2$	ϵ	Data/simulation	
		H$(e, e'p)$	H(e, e')
0.64	0.93	1.006 ± 0.005	1.015 ± 0.005
0.64	0.38	0.986 ± 0.005	0.997 ± 0.005
1.28	0.81	1.007 ± 0.005	1.009 ± 0.005
1.80	0.83	0.991 ± 0.005	1.003 ± 0.005
1.83	0.31	0.987 ± 0.005	0.989 ± 0.005
3.25	0.54	$0.94 \pm 0.012 \pm 0.06$	0.991 ± 0.007

ranges from $\sigma = 2.1$ MeV at $Q^2 = 0.64$ $(GeV/c)^2$ (backward angle) to $\sigma = 6.0$ MeV at $Q^2 = 1.8$ $(GeV/c)^2$ (forward angle).

The ratio of the observed to predicted *e-p* elastic scattering yield is shown in Table II. The typical systematic uncertainty for these measurements was 2.3%. However, the large uncertainty in the $(e, e'p)$ yield at $Q^2 = 3.25$ $(GeV/c)^2$ is due to an uncertainty in the proton efficiency due to malfunctioning wire chambers in the HMS. For all of the other points, including the single-arm electrons at 3.25 $(GeV/c)^2$, calculated and measured yields agree to within about 1%. The setting for $Q^2 = 3.25$ $(GeV/c)^2$ was the only one at which the protons were detected in the HMS and this efficiency problem was corrected before the data on the complex nuclei were taken.

At $Q^2 = 0.64$ $(GeV/c)^2$, there is little difference between the form factors obtained from Rosenbluth separations [9,10] and those from polarization transfer [11] and the form factors obtained from our measured cross sections at two values of epsilon are in agreement with both. At $Q^2 = 1.80$ $(GeV/c)^2$, where we also took data at two widely separated epsilons, the electric scattering contributes less than 20% of the cross section. The polarization transfer method only measures G_E/G_M [11,12] and so all that can be compared is the relative cross sections at the two epsilon points and at this Q^2 these differ by only 5%. Thus, while our measurements are in better agreement with previous Rosenbluth determinations our systematic uncertainties are too large for these results to be considered as evidence against the polarization transfer determinations. The Rosenbluth separation determinations are used in analyzing the present data and, where relevant, the implications of the results of [11] are noted.

Missing energy spectra for the nuclear targets

A missing energy and missing momentum spectrum were obtained at each data point for all three nuclear targets. These are the raw spectra from which the spectral functions were extracted after unfolding the radiative effects, the phase space weight, and the *e-p* cross-section weight. The raw missing energy spectra are shown in Figs. 3, 4, and 5.

Figure 3 shows the missing energy spectra for carbon. At $Q^2 = 0.64$ $(GeV/c)^2$ the spectra show a rather sharp peak corresponding to populating low-lying levels in ^{11}B which can be attributed to removing *p*-shell protons from ^{12}C and a
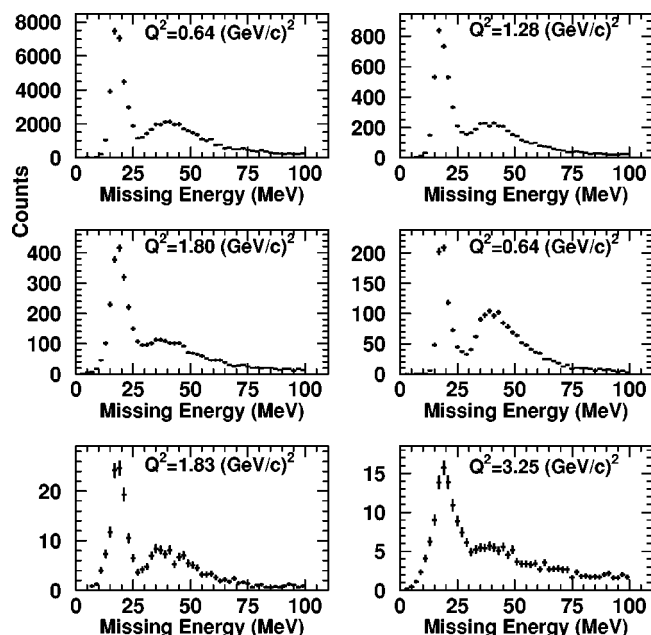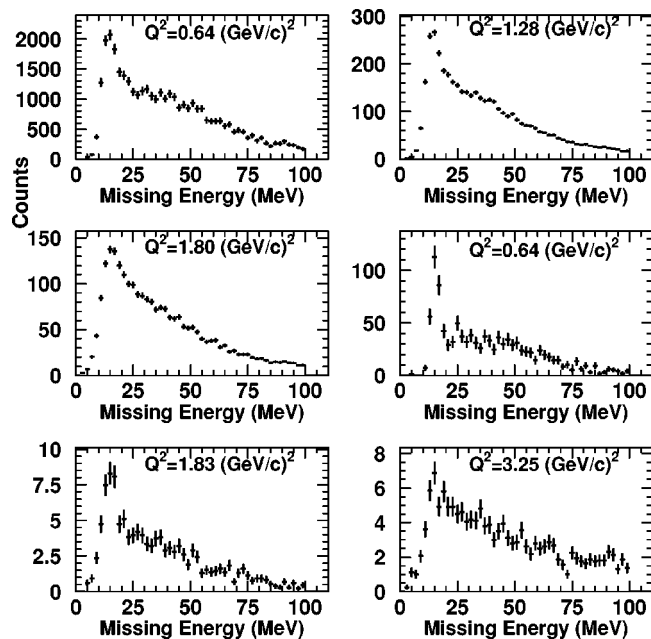
FIG. 3. Measured missing energy spectra for carbon at the different Q^2. The top left and middle right panels refer to the forward and backward electron angle kinematics, respectively, at $Q^2 = 0.64$ $(GeV/c)^2$ and the middle left and bottom left panels refer to the forward and backward electron angle kinematics, respectively, at $Q^2 = 1.80$ $(GeV/c)^2$. These are the *L-T* separation kinematics.

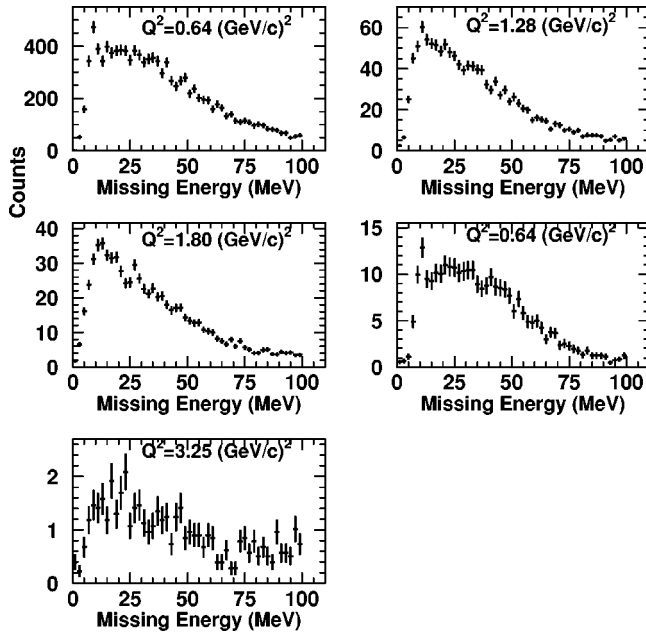FIG. 4. Measured missing energy spectra for iron at the different Q^2. The top left and middle right panels refer to the forward and backward electron angle kinematics, respectively, at $Q^2 = 0.64$ $(GeV/c)^2$ and the middle left and bottom left panels refer to the forward and backward electron angle kinematics, respectively, at $Q^2 = 1.80$ $(GeV/c)^2$. These are the *L-T* separation kinematics.

FIG. 5. Measured missing energy spectra for gold at the different Q^2. The top left and middle right panels refer to the forward and backward electron angle kinematics, respectively, at $Q^2=0.64$ (GeV/c)^2 and the middle left and bottom left panels refer to the forward and backward electron angle kinematics, respectively, at $Q^2=1.80$ (GeV/c)^2. These are the L-T separation kinematics.

broader peak at higher missing energies which is primarily due to removing s-shell protons. The missing momentum dependence of the spectral functions discussed below supports this identification. The valley between the two groups is increasingly filled in as Q^2 increases, because the (absolute) energy resolution broadens as the energy of the particles increases, as noted above in discussing the hydrogen spectra of Fig. 2. At the two values of Q^2 at which L-T separations were performed the valley between the s-shell and p-shell regions is less distinct at the forward electron angle, again reflecting the poorer energy resolution that was also observed in the hydrogen spectra. The missing energy spectra for iron are shown in Fig. 4. The ground-state region peak is more prominent at low Q^2 and backward angles. The missing energy spectra for gold are shown in Fig. 5. The statistical uncertainties are much poorer for gold than for the other targets and no trends are apparent.

Radiative and acceptance corrections

As previously noted, energy and momentum are lost by the electrons radiating photons in the Coulomb field of the target nucleus both before and after the scattering. The electrons can also emit bremsstrahlung radiation in passing through material in the spectrometers. The net result is a distortion of the spectra and the corrections to this distortion are model dependent. The code SIMC was used to generate correction factors for "deradiating" the observed spectral functions. Model spectral functions were used to populate bins in p_m and E_m space with both the radiative corrections turned on and turned off and the ratio was applied as a correction factor, bin by bin, to the spectral functions derived
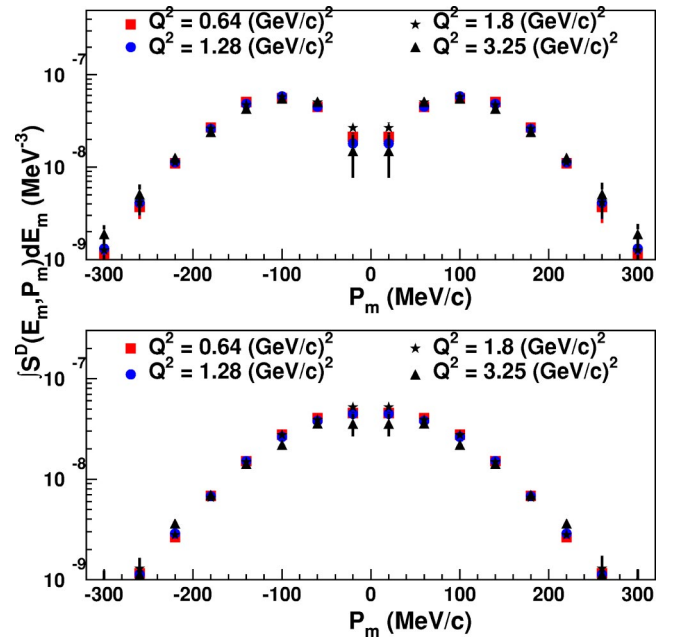

FIG. 6. (Color online) Momentum distributions for carbon p shell (top panel, $10 < E_m < 25$ MeV) and s shell (bottom panel, $30 < E_m < 50$ MeV). They have been normalized so that the integral of the measured spectral functions over $|p_m| < 300$ MeV/c is equal to the integral of the spectral function at Q^2 of 1.8 (GeV/c)^2.

from the experimental data. The Monte Carlo was also used to calculate the experimental phase space for each (E_m, p_m) bin. The experimental counts in each (E_m, p_m) bin corrected for radiation and divided by the phase space for that bin were used to obtain the "experimental" spectral function:

$$S^{\mathrm{derad}}(E_m, p_m) = \frac{1}{\mathcal{L} H(E_m, p_m)}$$

$$\times \sum_{\mathrm{counts}} \frac{1}{\sigma_{ep} E_{e'} p_{p'}(E_m, p_m)} C^{\mathrm{rad}}(E_m, p_m),$$

(9)

where $\mathcal{L}$ is the luminosity, $H(E_m, p_m)$ the phase space for the given E_m, p_m bin, $C^{\mathrm{rad}}(E_m, p_m)$ the correction factor for the same bin, and $\sigma_{ep} E_{e'} p_{p'}(E_m, p_m)$ the off-shell e-p cross section and kinematic factors averaged over the E_m and p_m bin. This "experimental" spectral function is then compared to the input model spectral function and if the two differ by more than a specified amount the experimental spectral functions become the new model spectral functions and the whole process is iterated until a satisfactory convergence is achieved. In order to test the validity of this procedure, nonphysical spectral functions were input as the model spectral functions and it was demonstrated that after several iterations the extracted spectral functions are virtually independent of the initial model function. The consistency of this deradiation procedure was also checked using Monte Carlo generated data. It should be noted that these corrected spectral functions still include distortions due to the effects of final state nuclear interactions, including absorption.
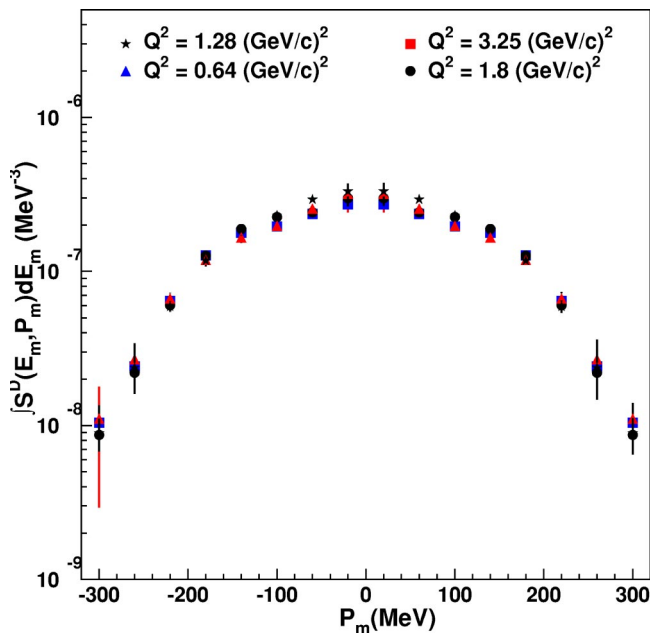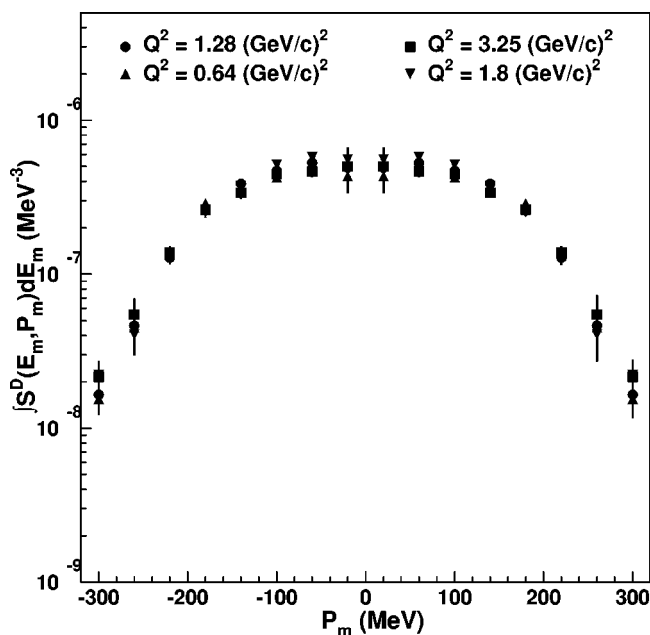
FIG. 7. (Color online) Momentum distributions for iron integrated over an E_m range $0 < E_m < 80$ MeV. They have been normalized so that the integral of the measured spectral functions over $|p_m| < 300$ MeV/c is equal to the integral of the spectral function at Q^2 of 1.8 (GeV/c)^2.

Experimental spectral functions

At each electron angle the above procedure was used for each proton angle to obtain experimental (distorted, as defined above) spectral functions and these were integrated over the proton angles to obtain the experimental spectral

FIG. 8. Momentum distributions for gold integrated over an E_m range $0 < E_m < 80$ MeV. They have been normalized so that the integral of the measured spectral functions over $|p_m| < 300$ MeV/c is equal to the integral of the spectral function at Q^2 of 1.8 (GeV/c)^2.
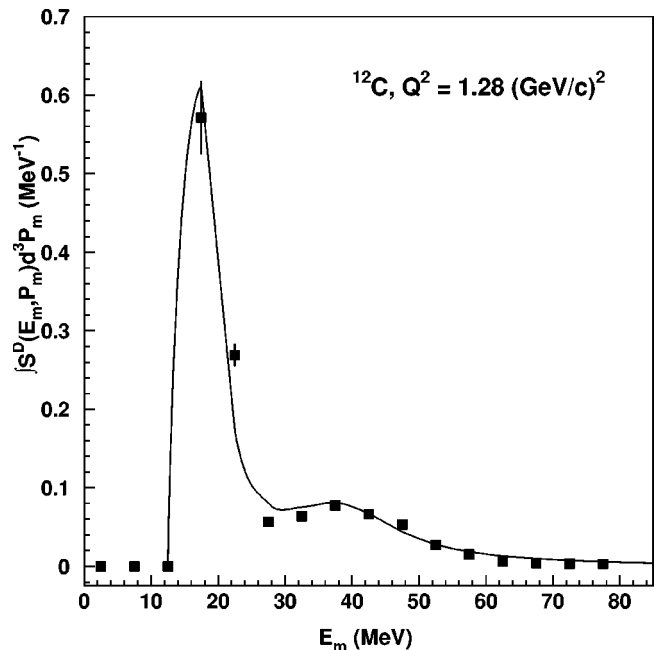
FIG. 9. Measured missing energy spectral function for carbon at $Q^2 = 1.28$ (GeV/c)^2 compared to independent particle shell model (IPSM).

functions for that target, electron angle, and Q^2. These summed spectral functions are functions of both missing momentum and missing energy and therefore the missing momentum was integrated over in order to obtain the energy spectral functions and the missing energy was integrated over to obtain momentum distributions. The momentum distributions are shown in Figs. 6, 7, and 8.

The carbon momentum distributions are shown in Fig. 6. They have been normalized to the spectral functions at Q^2 of 1.8 (GeV/c)^2 to remove the effect of variation in final state interactions between the different Q^2 points. These spectra show little variation with Q^2. The dip at zero missing momentum for missing energy between 10 and 25 MeV is attributable to the fact that the protons in this energy region are primarily $l=1$ while only $l=0$ protons can have zero missing momentum. There is a left-right (or $\pm$) asymmetry in the momentum distributions that is discussed below. As with carbon the iron momentum distributions (Fig. 7) and gold momentum distributions (Fig. 8) show little change with Q^2.

Independent particle shell model

Model spectral functions were calculated in the IPSM approximation, in which the nucleus is considered a sum of nucleons occupying distinct shells with each proton in the lowest possible shell. The parameters of the spectral function were adjusted to reproduce data from low-Q^2 $A(e,e'p)$ and $A(p,2p)$ experiments. For ^{12}C the removal energy and energy width of the two shells, $s_{1/2}$ and $p_{3/2}$, are based on the Saclay ^{12}C$(e,e'p)$ data [28]. The removal energy and energy width for the ^{56}Fe shells were based on the ^{58}Ni$(e,e'p)$ data from Saclay [28], with the removal energy corrected for the 2 MeV difference between ^{56}Fe and ^{58}Ni. The removal energy for the shells not resolved in the Saclay experiment
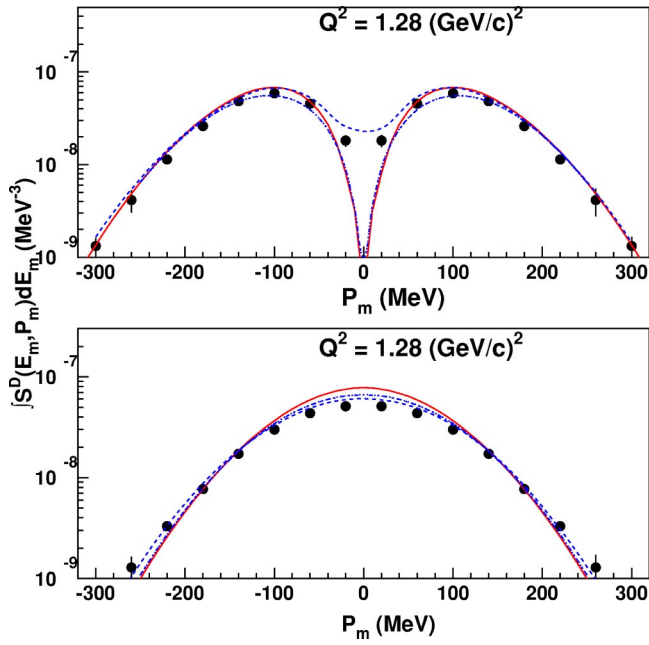
FIG. 10. (Color online) Measured momentum distribution for carbon at $Q^2 = 1.28$ (GeV/c)^2 in the p-removal energy region (top panel, $10 < E_m < 25$ MeV) and s-removal energy region (bottom shell, $30 < E_m < 50$ MeV) compared to theoretical predictions. The solid line is the IPSM; dashed line is IPSM with an 8% s-shell strength. Dotted line is a DWIA calculation from Zhalov et al. [36] and the dot-dashed line is the same DWIA calculation with color transparency included.

were obtained from Hartree-Fock calculations [29] and the widths for these shells were calculated according to the Brown and Rho [30] parametrization of data for $A < 58$. Similarly for ^{197}Au the removal energies and widths are based on those measured for nearby nucleus ^{208}Pb in $A(e, e'p)$ experiments at NIKHEF [29], with removal energies corrected for the 2.2 MeV difference between ^{208}Pb and ^{197}Au. The parameters for the unmeasured shells were obtained from Hartree-Fock calculations [29] and the Brown and Rho parametrization as mentioned above. Further details are given elsewhere [16].

Momentum distributions were obtained for each shell by solving the Schrödinger equation in a Woods-Saxon potential using the code DWEEPY [31]. For ^{12}C the parameters used in the potential were based on the Saclay ^{12}C$(e, e'p)$ data [28]. The ^{56}Fe and ^{197}Au momentum distributions were based on those measured for the nearby nucleus ^{58}Ni and ^{208}Pb, modified to agree with the ^{56}Fe$(e, e'p)$ and ^{197}Au$(e, e'p)$ data from SLAC experiment NE-18 [32], respectively. For ^{56}Fe and ^{197}Au a Perey factor (with $\beta = 0.85$) [33] was used to correct for the nonlocality or energy dependence of the potential.

The experimental missing energy spectral function for carbon at $Q^2 = 1.28$ (GeV/c)^2 is compared to the IPSM spectral function in Fig. 9. The model predicts slightly too much yield in the dip region between the $s_{1/2}$ and the $p_{3/2}$ shells possibly implying that the s shell is more tightly bound than generally thought. The momentum distribution (Fig. 10) in the region of the low missing energy peak, considered to be
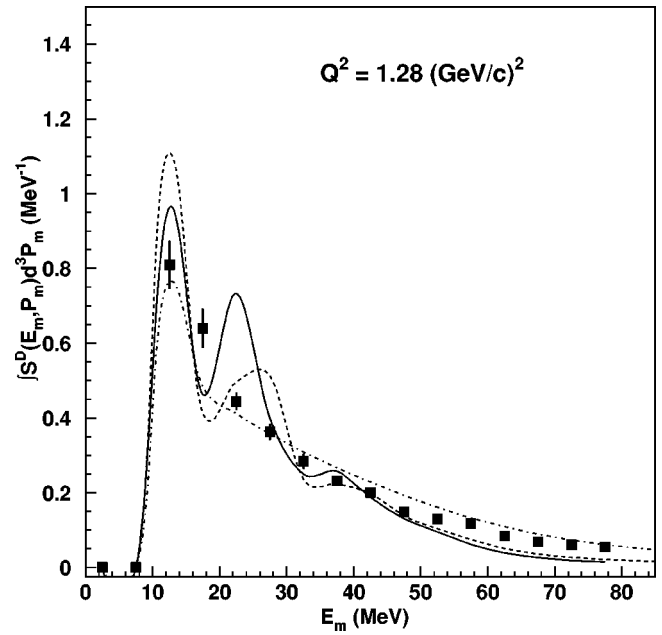

FIG. 11. Measured missing energy spectral function for iron at $Q^2 = 1.28$ (GeV/c)^2 compared to theoretical models. The solid line is drawn using the IPSM. The dashed line is a calculation from Benhar et al. [37] and the dot-dashed line is from calculations using the TIMORA code described in Ref. [38] with spreading widths taken from the IPSM.

the p-shell region, shows a much shallower minimum at $p_m = 0$ than the IPSM prediction, while for protons from the s-shell region the $p_m = 0$ yield is smaller than predicted. Agreement is much better if 8% of the s-shell strength is included (the E_m cut allows some s-shell strength into the p-shell region and vice versa). The spectroscopic factors
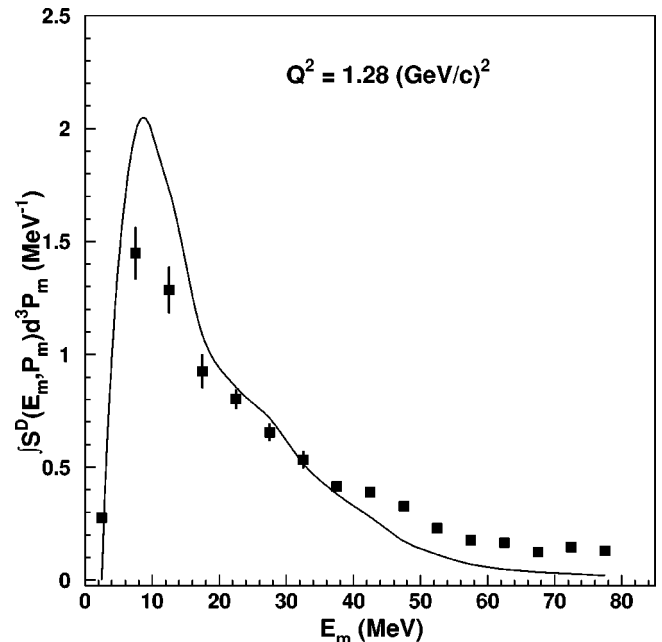

FIG. 12. Measured missing energy spectral function for gold at $Q^2 = 1.28$ (GeV/c)^2 compared to the IPSM.
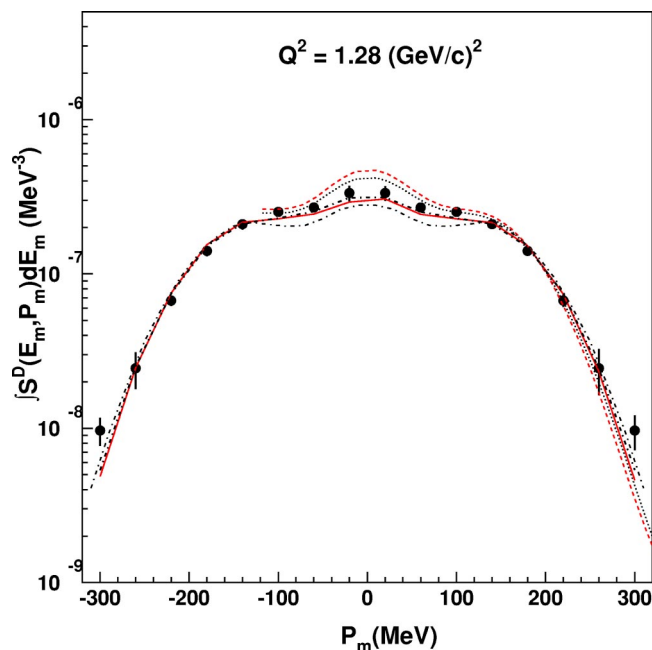
FIG. 13. (Color online) Measured momentum distribution for iron integrated over an E_m range $0 < E_m < 80$ MeV at $Q^2 = 1.28$ $(GeV/c)^2$, compared to theoretical predictions. Solid line is drawn using the IPSM. Dotted line is DWIA calculation from Zhalov *et al.* [36] without including color transparency and dot-dashed line is the same with color transparency included. Dot-dot-dash line is a calculation from Benhar *et al.* [37] and dash-dot-dash line is from calculations using the TIMORA code described in Ref. [38].

found in a high-resolution $(e, e'p)$ experiment done at NIKHEF [34] support the amount of s-p "mixing" invoked to explain the carbon missing momentum distributions.

The IPSM predicts sharper structure in the iron missing energy spectral functions (Fig. 11) than is observed, indicating that the shell widths are underestimated. Similar differences between calculation and experiment are seen in the gold data (Fig. 12). For both iron and gold the momentum spectral functions are fairly well predicted although in both cases the yield for $|p_m| > 250$ MeV/c is underpredicted, which is probably because the calculations underestimate the contribution from short-range correlations, two-body currents, and rescattering. It must be emphasized that in obtaining the transparencies, discussed in the following section, the data were integrated out to a missing energy of 80 MeV and therefore differences in spectral function structure between model and experiment are pretty well averaged out.

Other calculated spectral functions

Distorted wave impulse approximation (DWIA) calculations of the (distorted) spectral functions using the Hartree-Fock model with Skyrme's interaction to describe the single particle aspects of the nuclear structure [35] have been performed by Zhalov [36]. These calculations include an estimate of the effects of color transparency, which are negligible for carbon (Fig. 10) and barely discernible in iron (Fig. 13). These calculations overestimate the yield at small missing momentum and fall off too rapidly at large $|p_m|$. Spectral
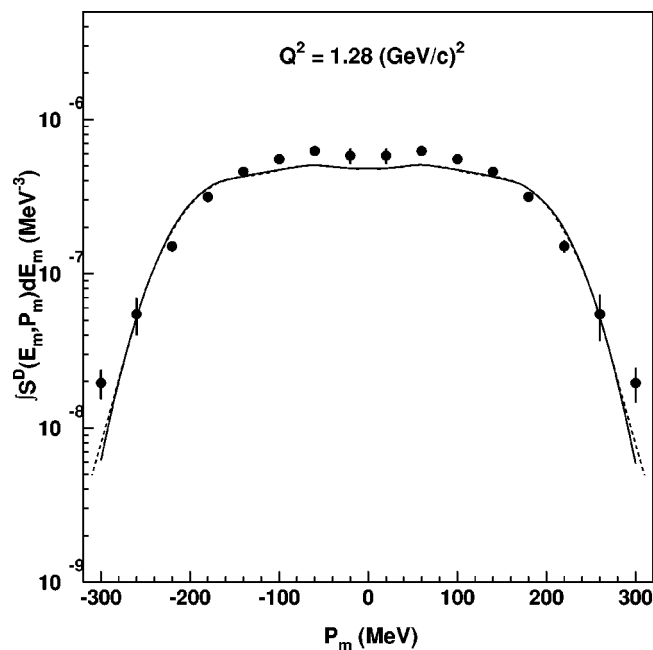

FIG. 14. Measured momentum distribution for gold integrated over an E_m range $0 < E_m < 80$ MeV at $Q^2 = 1.28$ $(GeV/c)^2$ compared to theoretical predictions. Solid line is drawn using the IPSM model and dashed line is a calculation from Benhar *et al.* [37].

functions have also been calculated by Benhar [37]. Here single-particle spectral functions are modified by adding terms dependent on the nuclear density. Results are shown in Fig. 13 (iron) and Fig. 14 (gold). Including the density dependence does increase the large p_m tail, though not by enough to reproduce the data. These calculations also underestimate the $p_m = 0$ region (it must be remembered that the momentum distribution is weighted by p_m^2 in normalizing calculation to experiment). The calculated energy spectral function for iron shows more structure than is observed, reflecting the fact that the IPSM spreading width was also used in the Benhar calculation (Fig. 11).

Energy and momentum distributions for iron have been calculated using the TIMORA code written by Horowitz [38] and based on the σ-ω mean-field theory of Walecka [39]. Details of this calculation are given elsewhere [40]. As can be seen in Fig. 11, this calculation gives a better fit to the observed structure, or lack thereof, than does either the IPSM or the Benhar [37] calculation.

Transparencies

As noted in the Introduction, the basic strategy used to obtain nuclear transparencies was to compare the measured yield to that calculated under the assumption that the struck proton escapes the nucleus without further interaction, i.e., the transparency is defined as the ratio of the measured yield to that calculated using the plane wave impulse approximation, or PWIA.

PWIA

For each target, incident electron energy, outgoing electron angle, and outgoing proton angle, the transparency was
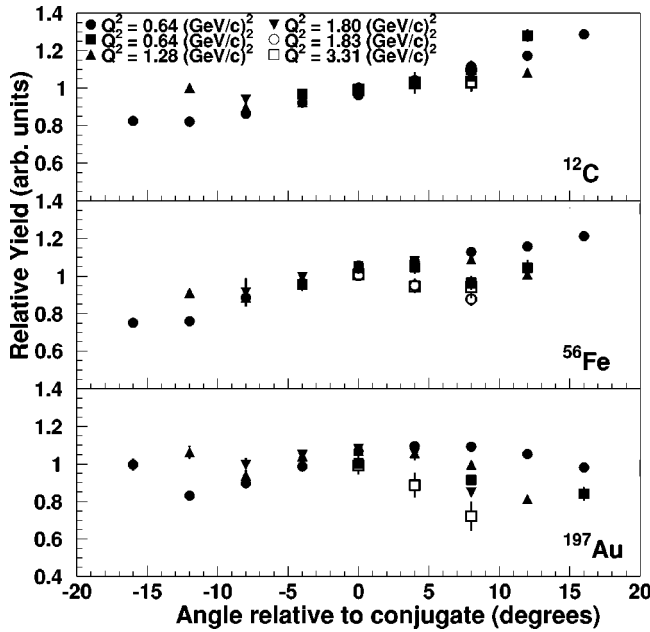
FIG. 15. Normalized transparency as a function of angle relative to the conjugate angle for carbon (top), iron (middle), and gold (bottom). Normalization was done at the conjugate angle. The solid circles and squares correspond to forward angle and backward angle kinematics, respectively, at $Q^2=0.64$ (GeV/c)^2.
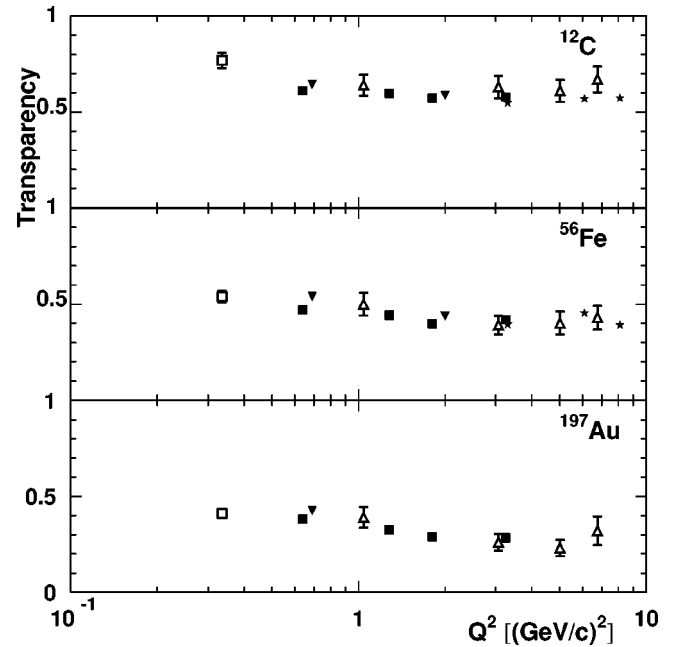

FIG. 16. Transparencies as a function of Q^2. The solid squares and triangles are from the present work and at both 0.64 and 1.8 (GeV/c)^2 one of the points is slightly offset so that the forward and backward angle (solid triangles) results can be shown separately. Also shown are results reported from experiments at Bates [1] (open square) and SLAC [2,3] (open triangle) and the followup to this experiment [4] (solid stars) at JLab.

determined as the ratio of the observed e-p coincidence yield, integrated over missing momentum (± 300 MeV/c) and missing energy (up to 80 MeV), to that calculated using the PWIA. However, before the expected coincidence e-p spectra in the absence of final state interactions can be calculated, a number of complications must be dealt with. As its name implies, the PWIA treats the incoming and outgoing particles as plane waves. There are, of course, the radiative corrections that are discussed above. Additionally, the incident and outgoing waves are distorted by the Coulomb field of the target and residual nucleus, respectively. It has been shown [38] that these distortions can be approximated by attaching a phase factor to the plane wave expansion. The acceleration by the Coulomb field increases the electron momentum k by

$$\delta k = f \frac{Z\alpha}{R}, \qquad (10)$$

where factor f varies between 1.1 and 1.5 depending on the size of the nucleus and R is the Coulomb radius of the

TABLE III. Transparencies found at the various Q^2 and ϵ for the three targets. Numbers in parentheses are statistical errors only.

Q^2 (GeV/c)^2	Carbon	Iron	Gold
0.64 (θ_e forward)	0.61(0.02)	0.47(0.01)	0.38(0.01)
0.64 (θ_e backward)	0.64(0.02)	0.54(0.01)	0.43(0.01)
1.28	0.60(0.02)	0.44(0.01)	0.32(0.01)
1.80 (θ_e forward)	0.57(0.01)	0.40(0.01)	0.29(0.01)
1.83 (θ_e backward)	0.59(0.01)	0.44(0.01)	
3.25	0.58(0.02)	0.42(0.01)	0.28(0.01)

nucleus. This can be used to estimate the effect of Coulomb distortion on the cross section with satisfactory accuracy [41]. This Coulomb acceleration of the electron necessitates using an effective momentum transfer and also alters the missing momentum [27]. All of these effects were incorporated into the PWIA and spectral function calculations.

The PWIA calculations were done using the "traditional" e-p free cross sections in which $\mu_p G_E/G_M \approx 1$. The fact that the target proton is moving and is bound to a nucleus (i.e., is "off shell") introduces considerable complications. Off-shell prescriptions for quasifree e-p cross sections have been given by deForest [25] and the prescription σ_{cc1} was used in the present work in calculating the PWIA cross sections. Another complication is the fact that the response function is no longer the incoherent sum of the longitudinal and transverse response functions but there are also the interference terms W_{LT} and W_{TT} [Eq. (2)]. The response function W_{LT} is antisymmetric about the conjugate, or free e-p scattering, angle and thus vanishes in this direction, known as "parallel kinematics." Of course, parallel kinematics is the only kinematics in free e-p scattering and the cross section is given by the familiar Rosenbluth formula.

While it is a reasonable first approximation to take complex nuclei as a collection of A nucleons moving in an average potential with orbits filled in order of increasing energy, this is too simplistic a picture to use in extracting transparencies. Short-range nucleon-nucleon correlations are present and one effect of these is to extend some single particle strength up to hundreds of MeV in E_m and well beyond the
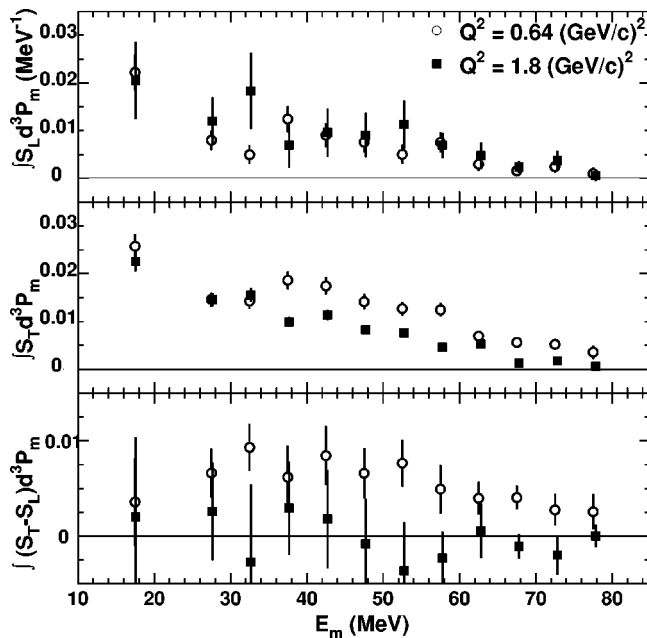
FIG. 17. Iron separated spectral functions integrated over a p_m range $0 < p_m < 80$ MeV/c. The $Q^2 = 1.8$ (GeV/c)^2 points have been displaced slightly for clarity. The lowest E_m point has been averaged over $10 < E_m < 25$ MeV. In obtaining these spectral functions the proton electric form factor was assumed to have the dipole form and the proton magnetic from factor was taken from Ref. [7].

FIG. 18. Gold separated spectral functions integrated over a p_m range $0 < p_m < 80$ MeV/c. In obtaining these spectral functions the proton electric form factor was assumed to have the dipole form and the proton magnetic from factor was taken from Ref. [7].

Fermi momentum in p_m. The missing energy spectra are indeed above the IPSM predictions at the high energy end but because of the acceptance cutoff of the spectrometers only a small portion of this "pushed-up" strength could be detected. Under the assumption that the correlations produce a uniform suppression of the spectral function below the Fermi momentum and the missing energy limit, correlation factors of 1.11 ± 0.03, 1.26 ± 0.08, and 1.32 ± 0.08 for carbon, iron, and gold, respectively, are calculated [42] and these corrections have been applied to the PWIA cross sections in extracting the transparencies.

Extracted transparencies

The apparent transparencies [i.e., ratio of measured to PWIA calculated $(e, e'p)$ coincidence yield] relative to that at the conjugate angle are shown in Fig. 15 for the carbon (top), iron (middle), and gold (bottom) targets, for the various electron kinematic settings. The transparencies are significantly asymmetric. One possible reason could be the presence of interference terms in the response function, i.e., a W_{LT} [Eq. (4)] in excess of that included in the deForest prescription σ_{cc1}. This is not unexpected because modern relativistic models predict such asymmetries [43,44]. However, it should be noted that Coulomb distortion of the electron waves can alter the effective scattering angle and therefore induce an asymmetry about the free conjugate angle. While much of the Coulomb distortion can be allowed for by introducing the momentum increase given by Eq. (10), it could well be that this correction is not adequate. Coulomb distortions are known to increase with Z [45].
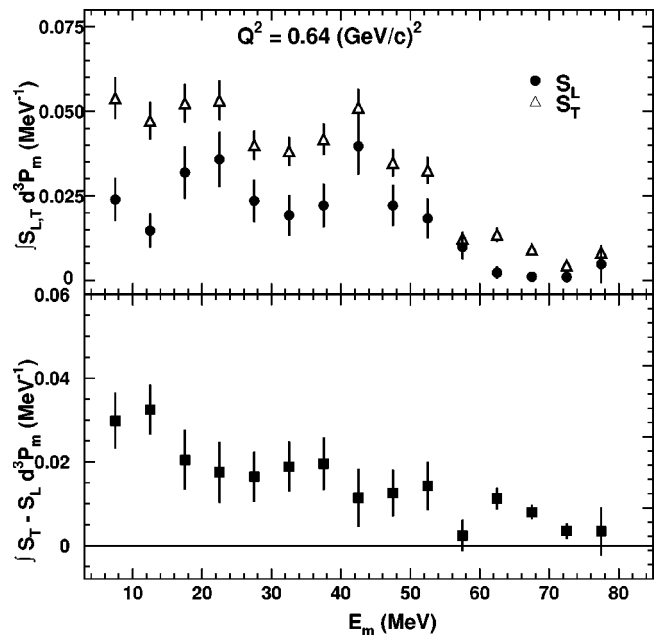
The angular dependence of the quasifree scattering depends directly on the momentum distribution of the scattering nucleons and the tendency of the transparency to peak at the conjugate angle that is seen in the iron and gold distributions could be due to an underestimate of the number of protons at large angles relative to the conjugate angle. None of these complications appear to be present in the carbon data and so we can conclude that in carbon at least there is evidence of an interference term in the response function that decreases with increasing Q^2. At the large proton angles relative to the conjugate angle there is a small contribution from other reaction mechanisms such as proton rescattering or $(e, e'n)$ followed by (n, p) charge exchange, but the yields are weak compared to the dominant quasifree strength [46,47].

The outgoing proton cone was integrated over in order to determine the transparency for that electron kinematic setting. The values thus obtained are shown in Table III and are plotted as a function of Q^2 for the various targets along with previous measurements in Fig. 16. There are three types of errors in the transparencies.

(i) Statistical: These are down in the 0.01 region and are never greater than 0.02.

(ii) Systematic: These are about 2.5% overall and about 2% from point to point.

(iii) Model dependence: These include uncertainties in the radiative corrections, the off-shell e-p cross sections, and the correlation corrections. The sum in quadrature of the model dependent uncertainties is about 5% for C and 8% for Fe and Au. The relative uncertainties in comparing different points with the same target are less than 5%.

In addition to the obvious trend of decreasing with increasing A, the transparencies also decrease with increasing Q^2, at least at the low end of the Q^2 range covered here. The
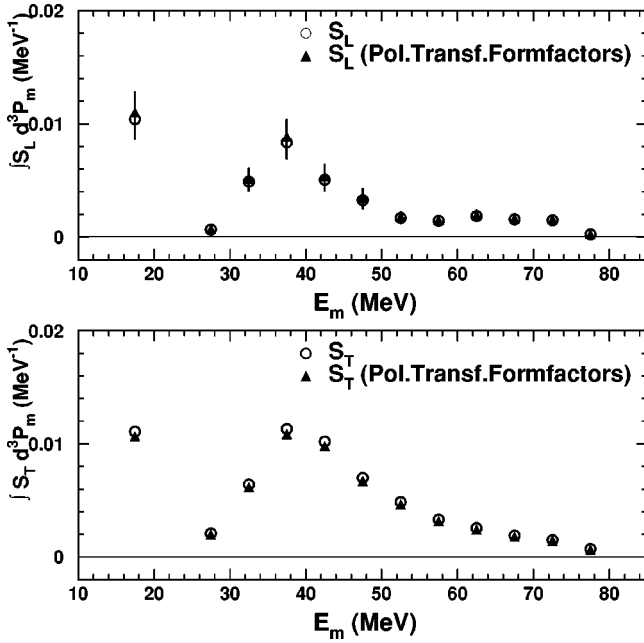
FIG. 19. Comparison of the carbon longitudinal (top panel) and transverse (bottom panel) spectral functions at $Q^2 = 0.64$ (GeV/c)^2, integrated over a p_m range $0 < p_m < 80$ MeV/c, using the proton form factors obtained by the Rosenbluth separation [9,10] (open symbols) and the polarization transfer [11] methods (solid symbols). The lowest E_m point has been averaged over $10 < E_m < 25$ MeV.

A and Q^2 dependence of the transparencies has already been described and discussed [5]. At the two values of Q^2 where data were taken at two different angles the transparency, as defined as the ratio of observed cross section to that predicted by the PWIA, is higher at the backward (i.e., high ϵ) angle. This is a manifestation of the enhancement of the transverse component of the cross section, discussed below in the section on the L-T separated spectral functions.

L-T separations

L-T separations were performed at 0.64 and 1.8 (GeV/c)^2. While at the low Q^2, small angle, point the entire cone of outgoing protons was covered just about as quickly as the spectrometer could be moved, because of the kinematic factors some compromises had to be made at the other settings. Performing L-T separations requires accurate data, partially because the anomalous proton magnetic moment leads to the response function being primarily transverse which, in turn, means that it is necessary to separate out a longitudinal response from a response function that is dominated by the transverse over the entire range. As noted above, except at the large ϵ, small Q^2 point it was not possible to cover the entire cone, which would have made it possible to average over the interference terms in the response function. The fact that the differential cross sections are not symmetric about the conjugate angle (Fig. 15) demonstrates that these terms are not necessarily negligible. For the L-T separations it was therefore decided to use only data where these terms must be small, namely, requiring that $|p_m|$ be less than 80 MeV/c.
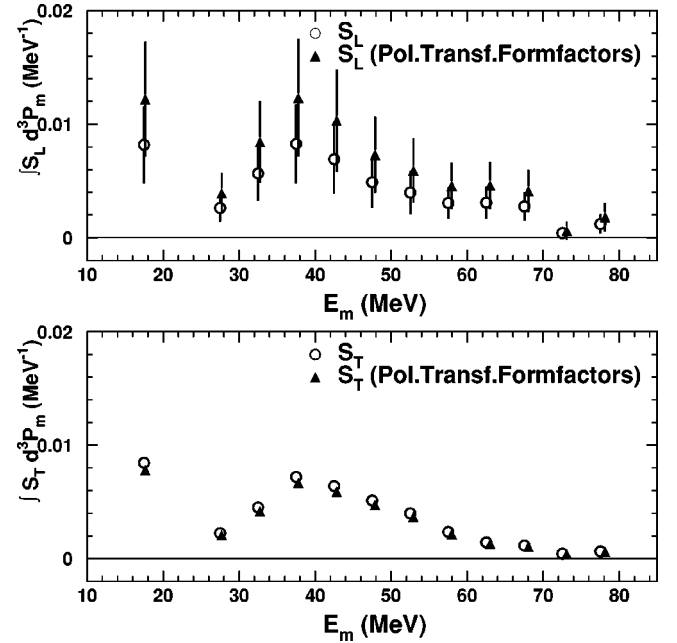

FIG. 20. Comparison of the carbon longitudinal (top panel) and transverse (bottom panel) spectral functions at $Q^2 = 1.8$ (GeV/c)^2, integrated over a p_m range $0 < p_m < 80$ MeV/c, using the proton form factors obtained by the Rosenbluth separation [9,10] (open symbols) and the polarization transfer [11] methods (solid symbols). The lowest E_m point has been averaged over $10 < E_m < 25$ MeV. The polarization transfer form factor points have been displaced slightly for clarity.

The spectral functions obtained using the PWIA are the weighted average of what can be called separated spectral functions, S_L and S_T, and can be written

$$S(E_m, \vec{p}_m) = \frac{\sigma_L S_L(E_m, \vec{p}_m) + \sigma_T S_T(E_m, \vec{p}_m)}{\sigma_L + \sigma_T}, \quad (11)$$

and the L-T separation then separates out S_L and S_T with the deForest prescription [25] used to modify σ_L and σ_T from the free nucleon values in order to account for the fact that the nucleons are bound in a nucleus. The separated spectral functions for carbon have already been reported [5]. Separated spectral functions for iron are shown in Fig. 17. Because of the increasing dominance of the magnetic scattering with increasing Q^2 [Eq. (1)] the errors in S_L increase with increasing Q^2 while the errors in S_T decrease somewhat. The transverse strength is clearly smaller at the higher Q^2 and, at 0.64 (GeV/c)^2, S_T is clearly greater than S_L. At $Q^2 = 1.8$ (GeV/c)^2, the errors on S_L are too great to allow any conclusions as to whether there are (relative) changes in S_L similar in magnitude to those found in S_T. Similar results were found for carbon [6].

An L-T separation for gold was only done at 0.64 (GeV/c)^2 and the resultant spectral functions are shown in Fig. 18. As with the other two targets at this momentum transfer, there is an excess of transverse strength.

The results described above were all obtained using the proton form factors with $\mu_p G_E \approx G_M$ as mentioned in the In-

troduction. Because the spectral functions are close to inversely proportional to the square of the form factors large changes in the form factors lead to large changes in the separated spectral functions. A comparison of the spectral functions obtained using the *L-T* separation [9,10] and the polarization transfer [11] form factors is shown in Fig. 19 (Fig. 20) for carbon at $Q^2=0.64$ (1.8) $(GeV/c)^2$. At 0.64 $(GeV/c)^2$ there is little effect on either spectral function and the substantial decrease in transverse strength at the higher Q^2 is still apparent. However, the form factors of Ref. [11] lead to a 60% increase in the longitudinal strength between the two values of momentum transfer. While the systematic errors of the present work are too large to require such a conclusion, mechanisms that would lead to such a Q^2 dependence are not obvious and it is clear that the final interpretation of the present (and a great deal of other) data must await a resolution of the question of the free proton electric form factor.

The behavior of the transverse spectral function as a function of Q^2 is consistent with a recent calculation of the separated cross sections on ^{16}O [48]. This calculation includes contribution from two-nucleon photoabsorption and predicts a reduction in the transverse strength with increasing Q^2, as observed in this experiment. However, it also predicts a large effect due to the two-nucleon photoabsorption on the longitudinal strength which is inconsistent with the present results. It should be pointed out that the effects due to two-nucleon photoabsorption calculated in Ref. [48] are an upper limit rather than an exact prediction.

CONCLUSIONS

Taking advantage of the high-quality electron beams and associated detection systems that have become available with JLab coming into operation, $(e,e'p)$ coincidence measurements were made on carbon, iron, and gold targets at momentum transfers Q^2 of 0.64, 1.28, 1.8, and 3.25 $(GeV/c)^2$. Spectral functions were measured for missing momentum out to 300 (GeV/c) and missing energy up to 80 MeV and these differ in detail, but not in overall shape, from independent particle shell model calculations. Other reported calculations do not give much better fits except those from a code based on a σ-ω mean field theory. By comparing the experimental yields integrated over missing energy and missing momentum with PWIA calculations nuclear transparencies for 350–1800 MeV protons were determined with an accuracy that is considerably greater than previously reported transparency determinations.

Longitudinal-transverse separations were performed at 0.64 $(GeV/c)^2$ and 1.8 $(GeV/c)^2$ with the iron and gold separations being the first such data on medium and heavy nuclei. Considerable excess transverse strength is found at $Q^2=0.64$ $(GeV/c)^2$ which is much reduced at 1.8 $(GeV/c)^2$. This excess strength is attributed to multinucleon effects that have less effect on smaller distance probes. Recently reported determinations of G_E/G_M for the proton which are in substantial disagreement with previously accepted values may, if they are confirmed, substantially alter the magnitude of the longitudinal spectral function at 1.8 $(GeV/c)^2$, but are within the systematic uncertainties of the present measurement. However, because G_M is primarily determined by the absolute cross section the transverse spectral function will be little affected.

[1] G. Garino *et al.*, Phys. Rev. C **45**, 780 (1992).

[2] T. G. O'Neill *et al.*, Phys. Lett. B **351**, 87 (1995).

[3] N. C. R. Makins *et al.*, Phys. Rev. Lett. **72**, 1986 (1994).

[4] K. Garrow *et al.*, Phys. Rev. C **66**, 044613 (2002).

[5] D. Abbott *et al.*, Phys. Rev. Lett. **80**, 5072 (1998).

[6] D. Dutta *et al.*, Phys. Rev. C **61**, 061602(R) (2000).

[7] M. Gari and W. Krümpelmann, Z. Phys. A **322**, 689 (1985).

[8] J. Arrington, Eur. Phys. J. A **17**, 311 (2003).

[9] R. C. Walker *et al.*, Phys. Rev. D **49**, 5671 (1994), and references cited therein.

[10] P. E. Bosted, Phys. Rev. C **51**, 409 (1994).

[11] M. K. Jones *et al.*, Phys. Rev. Lett. **84**, 1398 (2000).

[12] O. Gayou *et al.*, Phys. Rev. Lett. **88**, 092301 (2002).

[13] E. Offermann *et al.*, Phys. Rev. C **44**, 1096 (1991).

[14] F. Ajzenberg-Selove, Nucl. Phys. **A433**, 1 (1985).

[15] R. Hofstadter, Annu. Rev. Nucl. Sci. **7**, 231 (1957).

[16] D. Dutta, Ph.D. thesis, Northwestern University, 1999.

[17] D. Mack and C. Bochna, CEBAF Internal Report, 1997; C. Bochna, Ph.D. thesis, University of Illinois, 1999.

[18] F. Duncan, CEBAF Interal Report, 1996.

[19] J. R. Arrington, Ph.D. thesis, California Institute of Technology, 1998.

[20] R. Mohring, Ph.D. thesis, University of Maryland, 2000.

[21] S. Lassiter (private communication).

[22] M. Berz, NSCL Technical Report No. MSUSCL-977, Michigan State University, 1995.

[23] K. A. Assamagan, D. Dutta, and T. P. Welch, CEBAF Internal Report (unpublished).

[24] N. C. R. Makins, Ph.D. thesis, MIT, 1994.

[25] T. deForest, Jr., Nucl. Phys. **A392**, 232 (1983).

[26] L. W. Mo and Y. S. Tsai, Rev. Mod. Phys. **41**, 205 (1969).

[27] R. Ent, B. W. Filippone, N. C. R. Makins, R. G. Milner, T. G. O'Neill, and D. A. Wasson, Phys. Rev. C **64**, 054610 (2001).

[28] J. Mougey *et al.*, Nucl. Phys. **A262**, 461 (1976); S. Frullani and J. Mougey, Adv. Nucl. Phys. **14**, 1 (1982).

[29] J. W. Negele, Phys. Rev. C **1**, 1260 (1970); J. W. Negele and D. Vautherein, *ibid.* **5**, 1472 (1972); E. N. M. Quint, Ph.D. thesis, University van Amsterdam, 1988.

[30] G. E. Brown and M. Rho, Nucl. Phys. **A372**, 397 (1981).

[31] C. Giusti and F. D. Pacati, Nucl. Phys. **A473**, 717 (1987).

[32] T. G. O'Neill, Ph.D. thesis, California Institute of Technology, 1994.

[33] F. G. Perey, in *Direct Interactions and Nuclear Reaction Mechanisms*, edited by E. Ciemental and C. Villi (Gordon and Breach, New York, 1963).

[34] G. van der Steenhoven *et al.*, Nucl. Phys. **A484**, 445 (1988).

[35] L. L. Frankfurt *et al.*, Phys. Rev. C **50**, 2189 (1994).

[36] M. Zhalov (private communication); L. Frankfurt, M. Strikman, and M. Zhalov, Phys. Lett. B **503**, 70 (2001).

[37] O. Benhar (private communication); O. Benhar *et al.*, Eur. Phys. J. A **5**, 137 (1999).

[38] C. J. Horowitz, Nucl. Phys. **A368**, 503 (1981).

[39] J. D. Walecka, Ann. Phys. **83**, 491 (1974).

[40] D. van Westrum, Ph.D. thesis, University of Colorado, 1999.

[41] J. Knoll, Nucl. Phys. **A223**, 462 (1974).

[42] V. R. Pandharipande and S. C. Pieper, Phys. Rev. C **45**, 791 (1992).

[43] J. J. Kelly, Adv. Nucl. Phys. **23**, 75 (1996); Phys. Rev. C **60**, 044609 (1999).

[44] J. M. Udias *et al.*, Phys. Rev. C **48**, 2731 (1993); J. M. Udias *et al.*, *ibid.* **51**, 3246 (1995).

[45] M. van Batenburg, Ph.D. thesis, University of Utrecht, 2001.

[46] G. Van der Steenhoven *et al.*, Phys. Lett. B **191**, 227 (1987).

[47] S. Jeschonnek *et al.*, Nucl. Phys. **A570**, 599 (1994).

[48] J. Ryckebusch, Phys. Rev. C **64**, 044606 (2001).